Alumina 3-D Printed Wide-Angle Partial Maxwell Fish-Eye Lens Antenna

Petr Kaděra, *Member, IEEE*, Jesús Sánchez-Pastor, *Graduate Student Member, IEEE*, Masoud Sakaki, Rolf Jakoby, *Member, IEEE*, Niels Benson, *Member, IEEE*, Alejandro Jiménez-Sáez, *Member, IEEE*, and Jaroslav Lacik, *Member, IEEE*

***Abstract*—This letter presents a wide-angle partial Maxwell Fish-Eye (PMFE) lens antenna for W-band millimeter-wave communication, which is realized by alumina 3-D printing using lithography-based ceramic manufacturing. To achieve the targeted permittivity profile, in addition to structural measures, the solid-state porosity of alumina, and hence its material permittivity, is controlled by tuning the sintering temperature. The relative permittivity of bulk alumina was set at 5.13 with a sintering temperature of 1350 °C instead of being 9.2 with a sintering temperature of 1650 °C. The fabricated 3-D lens with a diameter of 33.7 mm achieves a peak realized gain of 25 dBi at a frequency of 109.5 GHz at the boresight, demonstrating a field-of-view of ±42° with a planar lens surface.**

***Index Terms*—Ceramics, lenses, lithography-based ceramic manufacturing, millimeter-wave communication, steerable antennas, 3-D printing.**

I. Introduction

WIDE-ANGLE lenses can be found in a large variety of applications, e.g., as an antenna for radar systems [1], space satellite communications [2], [3], reference radar targets and frequency-coded retroreflectors [4], [5], [6], power splitters [7], or invisible cloaking [8]. Typical representations of wide-angle lenses are Luneburg lenses [9], Gutman lenses [10], [11], Maxwell Fish-Eye (MFE) lenses [12], [13], [14], [15], [16], Eaton lenses [17], [18], or geodesic lenses [19]. Fabrication techniques for the aforementioned lenses vary from a full metallic implementation (bed-of-nails [20], groove gap waveguide [21], parallel plate waveguide [21]) to the lens realization using dielectric materials (3-D printing [23], mechanical or chemical micromachining [5], substrate integrated waveguides [1]).

Manuscript received 4 February 2024; revised 8 March 2024; accepted 12 March 2024. Date of publication 19 March 2024; date of current version 9 July 2024. This work was supported in part by the Internal Grant Agency of the Brno University of Technology under Project FEKT-S-23-8191 and in part by the German Research Foundation ("Deutsche Forschungsgemeinschaft") (DFG) under Project-ID 287022738 TRR 196 MARIE for Project C09. *(Corresponding author: Petr Kaděra.)*

Petr Kaděra and Jaroslav Lacik are with the Department of Radio Electronics, Brno University of Technology, Brno 612 00, Czechia (e-mail: kadera@vut.cz; lacik@vut.cz).

Jesús Sánchez-Pastor, Rolf Jakoby, and Alejandro Jiménez-Sáez are with the Institute of Microwave Engineering and Photonics, Technische Universität Darmstadt, 64283 Darmstadt, Germany (e-mail: jesus.sanchez@tu-darmstadt.de; jakoby@imp.tu-darmstadt.de; alejandro.jimenez_saez@tudarmstadt.de).

Masoud Sakaki and Niels Benson are with the Institute of Nanostructures and Technology, Universität Duisburg-Essen, 47057 Duisburg, Germany (e-mail: masoud.sakaki@uni-due.de; niels.benson@uni-due.de).

Digital Object Identifier 10.1109/LAWP.2024.3378754

In our work, we focus on the partial Maxwell Fish-Eye (PMFE) lens, which uses gradient permittivity profiles close to those of the Gutman and Eaton lens types, thus combining their functionality [12], [13]. Other examples of multifunctional lenses are bifunctional Luneburg/Eaton or Luneburg/MFE lenses, whose functionality is dependent on the electromagnetic (EM) wave propagation direction, as discussed in [24], [25]. The PMFE lenses presented in [12], [13] are functionally limited to the azimuthal plane, and their angular performance is strongly dependent on the dispersion characteristics of the used metallic structure geometry. Moreover, the practical realization of the wide-angle lenses operating in broadband frequency ranges and frequencies in the order of and over 100 GHz is often costly and highly demanding.

In this letter, we present an alternative PMFE lens approach based on exploiting lithography-based ceramic manufacturing (LCM) in combination with a specifically tuned sintering temperature (1350 °C). On the one hand, this allows us to design a 3-D broadband lens with large beam-steering capabilities in principal planes and with stable performance due to the use of a low-dispersive dielectric material [26]. On the other hand, the decrease of the alumina sintering temperature from 1650 °C to 1350 °C leads to a decreased bulk relative permittivity (ε_r) from 9.2 to 5.13 [27], which is beneficial for the realization of lenses requiring an ε_r in the order of 4 [10], [11], [12], [28], [29]. A similar effect of the influence of sintering temperature on the material bulk permittivity was reported for zirconia in [30]. Other benefits of employing alumina as the selected material are operational sustainability in high-temperature environments [31], strong chemical and radiation resistance demanded e.g., space applications [32], [33], low-loss and stable permittivity [26] over a very broadband frequency range limited only by the effective medium theory linearity [34], and fine porosity, which leads to the absence of a photonic crystal electromagnetic bandgap (EBG) in the considered frequency range [35].

II. 3-D Partial Maxwell Fish-Eye Lens

The MFE lens is a rotationally symmetric device that transforms a spherical wave at its focal point to the focal point located on the opposite side of the lens, acting as a mirror [36]. The MFE lens can be compared to the Luneburg lens when it is cut in half [15]. The MFE gradient permittivity profile (1) follows

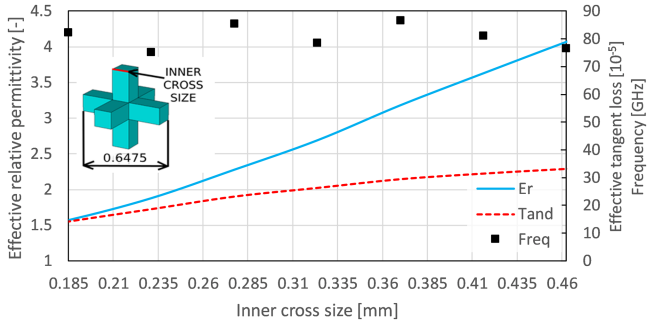

Fig. 1. Effective relative permittivity and effective tangent loss of cross-based unit cell after sintering and the frequency at which they are obtained.

the distribution given by:

$$\varepsilon_{\mathrm{r,eff}} = \frac{4}{\left(1+\left(\frac{r}{R}\right)^2\right)^2} \tag{1}$$

where $\varepsilon_{\mathrm{r,eff}}$ is the effective relative permittivity, r is the radial position, and R is the lens radius.

A. MFE Lens Permittivity Profile Discretization

To realize the targeted MFE permittivity profile by 3-D printing using the LCM technique, a suitable discretization has to be applied. Based on our previous analysis of 3-D printed unit cells in [4], a cross-based unit cell with dimensions of 0.6475 $\times$ 0.6475 $\times$ 0.6475 mm^3 is selected for the lens discretization. The lens diameter is set to 33.7 mm. This value is limited by the maximum size of the printable green body, which is 64 $\times$ 40 $\times$ 100 mm^3. The expected shrinkage is 7.5 % in the *XYZ* directions [27], so that means that the diameter of the printed green body, with the aforementioned value, will be 36.4 mm, close to the maximum possible value.

The determined bulk relative permittivity of the alumina sintered at 1350 °C is 5.13, with a tangent loss of 3.65 $\times$ 10^{-4} at 100 GHz [27]. Then, the achievable effective relative permittivity ($\varepsilon_{\mathrm{r,eff}}$) and effective tangent loss ($\tan\delta_{\mathrm{eff}}$) for varying inner cross sizes of a cubic unit cell are obtained from the dispersion analysis described in [37] and [38]. The resulting effective parameters and their corresponding frequencies are shown in Fig. 1. The minimum inner cross size of the green body is set to 0.2 mm, owing to the stability of the structure, resulting in 0.185 mm after sintering. To avoid an excessive ceramic/photopolymer resin residue in the fabricated lens structure, as reported in our previous works [4], [23], the maximum inner cross size of the green body is limited to 0.5 mm, resulting in 0.46 mm after sintering. The discretized ideal and 3-D printed $\varepsilon_{\mathrm{r,eff}}$ profile of the MFE lens is depicted in Fig. 2.

B. Full-Wave Numerical Simulation

To verify the performance of the ideal MFE lens, a full-wave time-domain analysis in CST Studio Suite is performed at the W-band (75–110 GHz), with a WR-10 waveguide feed and the model discretized into rotational symmetric rings. In the next step, the lower part of the original MFE lens is cut away to create a planar surface for the feeding waveguide. The optimal position of the cut is found as a compromise between the maximization

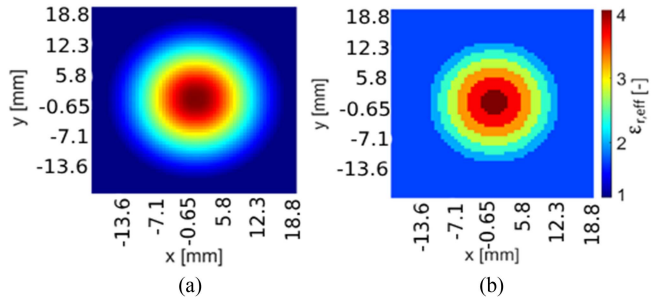

Fig. 2. (a) 2-D discretized effective relative permittivity profile of the ideal and (b) 3-D printed MFE lens.

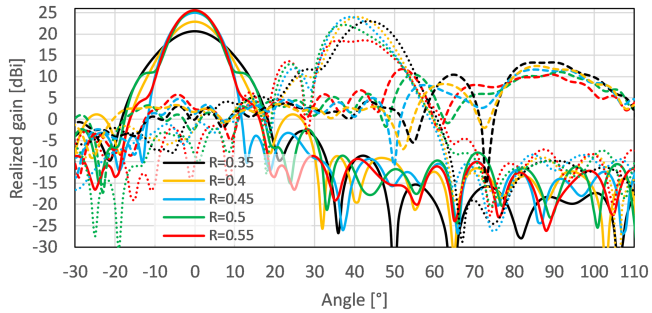

Fig. 3. Simulated realized gain of the PMFE lens antenna from cylindrical rings at different waveguide feeding (0 mm - solid; 6 mm - dotted; 13 mm - dashed) and cut positions at 80 GHz.

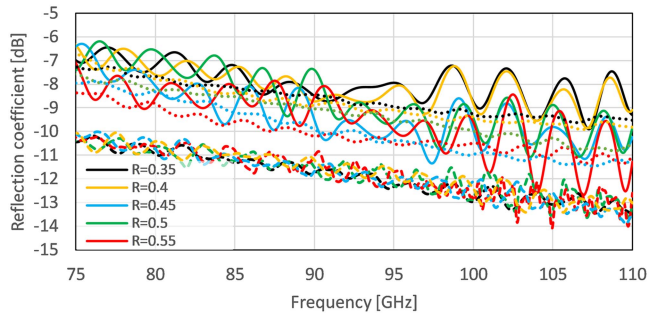

Fig. 4. Simulated reflection coefficient of the MFE lens antenna from cylindrical rings at different waveguide feeding (0 mm - solid; 6 mm - dotted; 13 mm - dashed) and cut positions.

of the lens antenna gain at its center and its edge positions, as depicted in Fig. 3. The works in [12] and [13] suggest cutting the lens at the position of 0.45*R* in the bed-of-nails and dielectric-filled PPW configurations, to achieve a maximum in beam-steering capabilities. However, such implementations are highly dispersive over frequency due to the use of metallic parts, which is in contrast to a low-dispersive dielectric unit cell design used in this work.

In our analysis, we sweep the lens cut position from 0.35*R* to 0.55*R* and evaluate the PMFE lens performance at the center, middle and edge positions (0, 6, and 13 mm) of the lens bottom to find an optimum between the maximum gain at the center and the edge positions. The achieved simulated realized gain and reflection coefficient are presented in Figs. 3 and 4. The electric field demonstrating EM wave propagation through the MFE and PMFE lenses is depicted in Fig. 5.

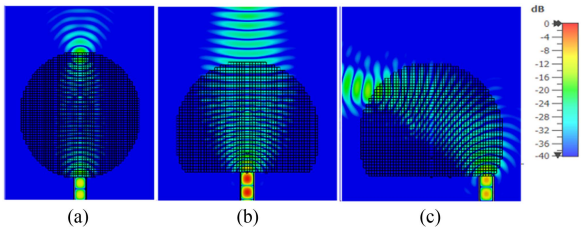

Fig. 5. Electric field distribution of (a) MFE lens, PMFE lens cut at 0.45R at (b) the center, and (c) the edge position at 80 GHz.

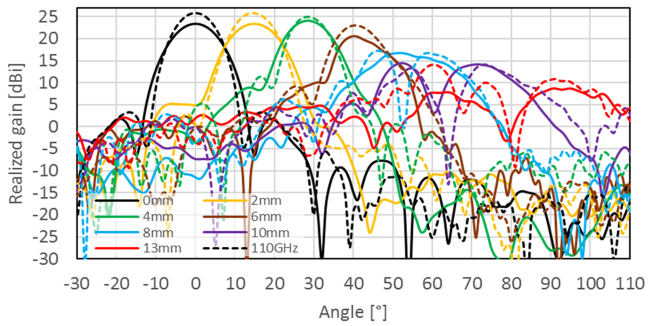

Fig. 6. Simulated radiation pattern of the PMFE lens antenna from cross-based unit cells at different waveguide feeding positions at 80 GHz (solid) and 110 GHz (dashed).

The best results are achieved for the lens cut position at 0.45R, leading to the antenna realized gain of 25 dBi and 11.3 dBi at the lens center and edge positions, respectively, at the design frequency of 80 GHz. The reflection coefficient is better than −6.3 dB in the whole W-band. To improve the reflection coefficient of the PMFE lens antenna, the addition of an impedance matching layer (IML) [3], [4] is feasible. However, two important concerns have to be further addressed. First, adding an IML will change the optimal lens cut position, and the maximum gain and beam steering angle will be reduced. Second, to compensate for this effect, modification of the MFE lens permittivity distribution will be required to find a new optimum between the maximum gain at the center and the edge positions.

The simulated realized gain of the PMFE lens antenna created from cross-based unit cells at different waveguide feeding positions is shown in Fig. 6. It is noticeable that the maximum 90° beam steering is reached at the edge position. The expected antenna field-of-view (FoV), defined as −3 dB drop in gain, is ±42°.

C. Lens Fabrication and Characterization

The PMFE lens was fabricated via the LCM method using a Lithoz CeraFab-7500 printer and LithaLox360 photosensitive slurry, with a pixel size of 25 μm in X-, Y-, and Z- directions. After printing, the green PMFE lens was cleaned by LithaSol 20 cleaning solution to remove the excess of slurry. The sample was then slowly heated to remove the polymer from the system and to yield the alumina samples with the desired permittivity. In this study, the sintering temperature and dwell time were 1350 °C for 2 h. More details about this process can be found in our previous work [4]. The structure of the fabricated lens is shown in Fig. 7.

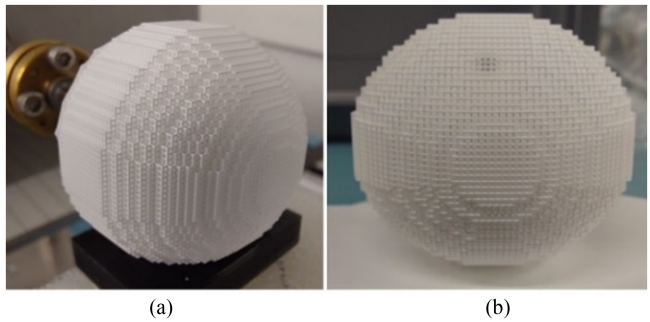

Fig. 7. Fabricated PMFE lens from (a) side and (b) top view.

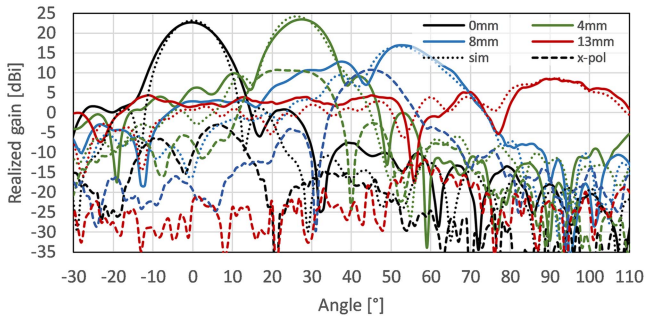

Fig. 8. Measured (co-pol solid, x-pol dashed) and simulated (dotted) radiation patterns of the PMFE lens antenna at different waveguide feeding positions at 80 GHz.

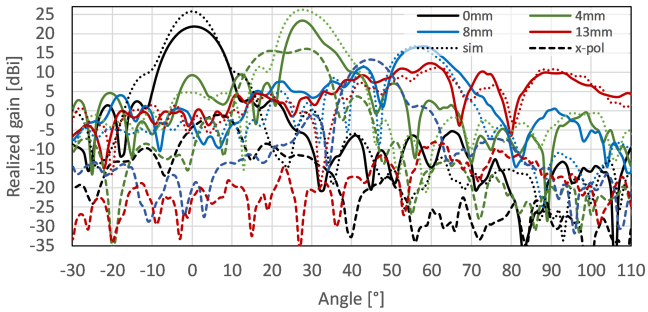

Fig. 9. Measured (co-pol solid, x-pol dashed) and simulated (dotted) radiation patterns of the PMFE lens antenna at different waveguide feeding positions at 110 GHz.

The lens antenna parameters and radiation patterns were measured employing the Vector Network Analyzer R&S ZVA67 with R&S ZVA-Z110E frequency convertors. The lens rotation was computer-controlled in 1° steps. Figs. 8–11 show the measured and simulated results of cross-based PMFE lens antenna: radiation patterns with lens holder in H-plane, broadband realized gain at different waveguide feeding positions, aperture efficiency, and reflection coefficients. The measured antenna aperture efficiency is below 30%, mainly owing to the selected lens cut position, the directivity of the feeding waveguide, and nonideal impedance matching of the planar lens surface, also reported in [3] and [28], albeit for other types of lens. Further, the conductivity loss in the feeding waveguide and the dielectric loss in alumina have rather minor effects. Note that a part of

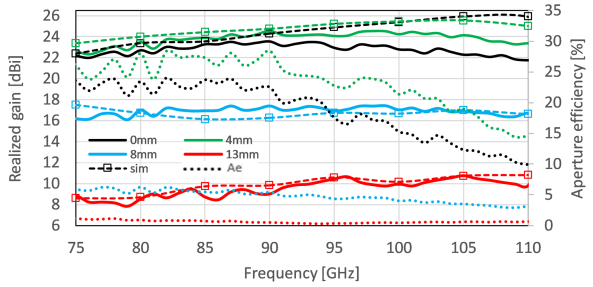

Fig. 10. Measured (solid) and simulated (dashed) broadband realized gain and measured aperture efficiency (dotted) of the PMFE lens antenna at different waveguide feeding positions.

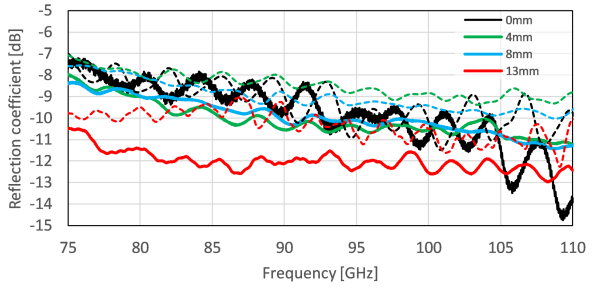

Fig. 11. Measured (solid) and simulated (dashed) reflection coefficient of the PMFE lens antenna at different waveguide feeding positions.

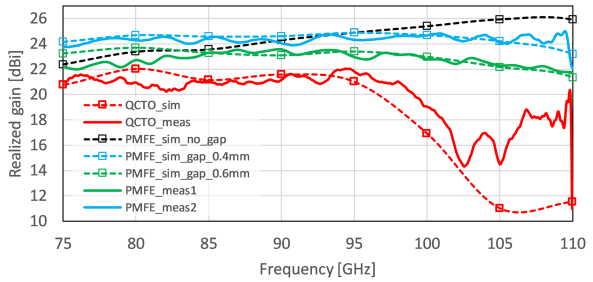

Fig. 12. Measured and simulated broadband realized gain of the PMFE and QCTO Luneburg [4] lens antenna at boresight, including a gap effect.

the beam energy misfocus for the waveguide feeding positions closer to the lens edge [Fig. 5(c)].

The simulated maximum operational frequency of the PMFE lens antenna designed from the cross-based unit cells (Fig. 12) is characterized by the 1 dB gain drop at around 110 GHz. This is a 15 GHz improvement (caused by the decrease of alumina's bulk permittivity), when compared to the quasi-conformal transformation optics (QCTO) Luneburg lens discussed in a previous contribution, which was realized from conventionally sintered alumina, with an ε_r of 9.52 and designed with the same unit cell constraints [4]. The simulated maximum operational frequency for the given cross-based unit cell corresponds to the half-wavelength resonances in the effective medium (photonic crystal EBG). Nevertheless, the effect can differ depending on the unit cell shape [39]. Even though nonideal lens alignment and a gap between the lens and the waveguide, the measured maximum operational frequency reaches 110 GHz for the PMFE lens, compared to the 98 GHz of the QCTO Luneburg lens. The

TABLE I
PARTIAL MFE LENS PARAMETERS AT THE FREQUENCIES OF 80/110 GHZ

80 GHz				
Position [mm]	Realized gain sim [dBi]	Realized gain meas [dBi]	Reflection coefficient sim/meas [dB]	Beam steering angle sim/meas [°]
0	23.38	24.28	-8.77/-8.37	0/0
4	23.99	23.49	-8.02/-9.01	26/27
8	16.72	16.99	-8.07/-8.98	52/53
13	8.69	8.53	-9.49/-11.45	92/91
110 GHz				
Position [mm]	Realized gain sim [dBi]	Realized gain meas [dBi]	Reflection coefficient sim/meas [dB]	Beam steering angle sim/meas [°]
0	25.90	22.05	-9.77/-13.72	0/1
4	25.01	23.39	-8.81/-11.23	28/28
8	16.75	16.71	-9.61/-11.28	56/59
13	10.78	9.81	-10.05/-12.43	91/89

TABLE II
COMPARISON OF W-BAND BEAM SCANNING LENS ANTENNAS

Ref.	Lens type	Peak realized gain [dBi]	Field -of-View [°]	Max. operational frequency [GHz]	Dimensions [λ_{f_max}]
[1]	SIW Luneburg	15.38	± 85	83	6.3 x 1
[4]	3D printed QCTO Luneburg	22	± 65	98	9.7 x 9.7 x 7.5
[40]	Integrated metal-based	31	< ± 30	79	17.2 x 17.2 x 11.9
[41]	3D printed Luneburg	24.8	± 20	110	7.3 x 7.3 x 7.3
[42]	Rotman	14	± 30	110	n/a
This work	3-D printed partial MFE	25	± 42	110	12.4 x 12.4 x 9

abrupt change of measured gain close to 110 GHz is caused by the window used for time-gating during signal post processing and does not represent the lens' response. The effect of a gap between the lens and excitation waveguide on the broadband antenna gain is documented in Fig. 12, where we can observe that the proper alignment between both parts is critical, since the gap between them influences the maximum gain due to the shift of the focal point and decreases the impedance matching.

A summary of achieved parameters is documented in Table I and a comparison to other related works is presented in Table II. The maximum operational frequency is defined by a reflection coefficient below −10 and 1 dB drop from the maximum gain at the broadside.

III. CONCLUSION

In this letter, we propose a 3-D partial MFE lens antenna realized in alumina by ceramic-based additive manufacturing. We demonstrate that a low sintering temperature of 1350 °C can be exploited to realize gradient index lenses with a maximum relative permittivity value close to 4, which is beneficial for modern wide-angle lens antenna designs. The fabricated lens exhibits a realized peak boresight gain of 25 dBi at 109.5 GHz and FoV of ±42°, with the possibility to steer the beam up to ±90°, although with a high scanning loss. This overcomes the achieved maximum operating frequency for current unit cell-based high-permittivity QCTO Luneburg lenses realized using LCM technology with standard processing. Moreover, compared with other lenses in literature in the W-band, it presents either a higher operating frequency, up to 110 GHz, or a wider FoV.

ACKNOWLEDGMENT

The authors acknowledge the Open Access support provided by Brno University of Technology.

REFERENCES

[1] M. K. Saleem, H. Vettikaladi, M. A. S. Alkanhal, and M. Himdi, "Lens antenna for wide angle beam scanning at 79 GHz for automotive short range radar applications," *IEEE Trans. Antennas Propag.*, vol. 65, no. 4, pp. 2041–2046, Apr. 2017.

[2] N. Garcia and J. Chisum, "Compound GRIN lens fanbeam antenna for wide-angle scanning," in *Proc. IEEE Int. Symp. Antennas Propag. USNC-URSI Radio Sci. Meeting*, 2021, pp. 1819–1820, doi: 10.1109/APS/URSI47566.2021.9703979.

[3] S. Biswas and M. Mirotznik, "High gain, wide-angle QCTO-enabled modified Luneburg lens antenna with broadband anti-reflective layer," *Sci. Rep.*, vol. 10, Jul. 2020, Art. no. 12646.

[4] P. Kaděra et al., "Wide-angle ceramic retroreflective Luneburg lens based on quasi-conformal transformation optics for mm-wave indoor localization," *IEEE Access*, vol. 10, pp. 41097–41111, 2022.

[5] P. Kadera et al., "Sub-THz Luneburg lens enabled wide-angle frequency-coded identification tag for passive indoor self-localization," *Int. J. Microw. Wireless Technol.*, vol. 15, no. 1, pp. 59–73, 2023.

[6] P. Kadera, A. Jiménez-Sáez, T. Burmeister, J. Lacik, M. Schüßler, and R. Jakoby, "Gradient-index-based frequency-coded retroreflective lenses for mm-wave indoor localization," *IEEE Access*, vol. 8, pp. 212765–212775, 2020.

[7] Q. Lei, R. Foster, P. S. Grant, and C. Grovenor, "Generalized Maxwell fish-eye lens as a beam splitter: A case study in realizing all-dielectric devices from transformation electromagnetics," *IEEE Trans. Microw. Theory Techn.*, vol. 65, no. 12, pp. 4823–4835, Dec. 2017, doi: 10.1109/TMTT.2017.2727495.

[8] L. Zhao and M. Yu, "Structural luneburg lens for broadband cloaking and wave guiding," *Sci. Rep.*, vol. 10, 2020, Art. no. 14556.

[9] R. K. Luneburg and M. Herzberger, *Mathematical Theory of Optics*. Berkeley, CA, USA: Univ. Calif. Press, 1964, pp. 182–188.

[10] P. Bantavis, C. G. Gonzalez, R. Sauleau, G. Goussetis, S. Tubau, and H. Legay, "Broadband graded index Gutman lens with a wide field of view utilizing artificial dielectrics: A design methodology," *Opt. Exp.*, vol. 28, pp. 14648–14661, 2020.

[11] O. Zetterstrom, N. J. G. Fonseca, and O. Quevedo-Teruel, "Additively manufactured half-Gutman lens antenna for mobile satellite communications," *IEEE Antennas Wireless Propag. Lett.*, vol. 22, no. 4, pp. 759–763, Apr. 2023, doi: 10.1109/LAWP.2022.3224455.

[12] H. Lu, Z. Liu, Y. Zhang, K. Pang, and Y. Liu, "Partial Maxwell fish-eye lens inspired by the Gutman lens and Eaton lens for wide-angle beam scanning," *Opt. Exp.*, vol. 29, no. 15, pp. 24194–24209, 2021.

[13] P. Zhen, B. Nie, H. Lu, Y. Liu, Y. Zhang, and X. Lv, "E-plane-focused partial Maxwell fish-eye lens antenna for multibeam wide-angle scanning," *IEEE Antennas Wireless Propag. Lett.*, vol. 22, no. 8, pp. 1853–1857, Aug. 2023, doi: 10.1109/LAWP.2023.3266580.

[14] D. Headland, M. Fujita, and T. Nagatsuma, "Half-Maxwell fisheye lens with photonic crystal waveguide for the integration of terahertz optics," *Opt. Exp.*, vol. 28, no. 2, pp. 2366–2380, 2020.

[15] J. M. Poyanco, F. Pizarro, and E. Rajo-Iglesias, "3D-printed half-Maxwell fish-eye dielectric lens antenna with integrated DRA feed," in *Proc. 16th Eur. Conf. Antennas Propag.*, 2022, pp. 1–5, doi: 10.23919/EuCAP53622.2022.9769238.

[16] S. Yang, Q. Chen, F. Mesa, N. J. G. Fonseca, and O. Quevedo-Teruel, "Geodesic half-Maxwell fish-eye-lens antenna," *IEEE Trans. Antennas Propag.*, vol. 71, no. 3, pp. 2330–2338, Mar. 2023, doi: 10.1109/TAP.2023.3240333.

[17] M. Yin, X. Y. Tian, L. L. Wu, and C. D. Li, "All-dielectric three-dimensional broadband Eaton lens with large refractive index range," *Appl. Phys. Lett.*, vol. 104, 2014, Art. no. 094101.

[18] S.-H. Kim, "Analytic solution of the generalized Eaton lens," *J. Modern Opt.*, vol. 68, no. 3, pp. 143–145, 2021.

[19] O. Quevedo-Teruel et al., "Geodesic lens antennas for 5G and beyond," *IEEE Commun. Mag.*, vol. 60, no. 1, pp. 40–45, Jan. 2022, doi: 10.1109/MCOM.001.2100545.

[20] C. D. Paola, K. Zhao, S. Zhang, and G. F. Pedersen, "A novel lens antenna design based on a bed of nails metasurface for new generation mobile devices," in *Proc. 14th Eur. Conf. Antennas Propag.*, 2020, pp. 1–5, doi: 10.23919/EuCAP48036.2020.9135354.

[21] D. Pérez-Quintana et al., "Fully metallic luneburg metalens antenna in gap waveguide technology at V-band," *IEEE Trans. Antennas Propag.*, vol. 71, no. 4, pp. 2930–2937, Apr. 2023, doi: 10.1109/TAP.2023.3243277.

[22] Y. Amarasinghe et al., "Broadband wide-angle terahertz antenna based on the application of transformation optics to a Luneburg lens," *Sci. Rep.*, vol. 11, 2021, Art. no. 5230.

[23] P. Kadera and J. Lacik, "Performance comparison of W-band Luneburg lens antenna: Additive versus subtractive manufacturing," in *Proc. 20th Int. Conf. Microw. Techn.*, 2021, pp. 1–6, doi: 10.1109/COMITE52242.2021.9419879.

[24] X. Li et al., "Bifunctional /luneburg-Eaton lens fabricated of 3-D-printed anisotropic medium," *IEEE Antennas Wireless Propag. Lett.*, vol. 21, no. 7, pp. 1462–1466, Jul. 2022, doi: 10.1109/LAWP.2022.3171777.

[25] J. Chen, Y. Zhao, L. Xing, Z. He, and L. Sun, "Broadband bifunctional Luneburg–fisheye lens based on anisotropic metasurface," *Sci. Rep.*, vol. 10, 2020, Art. no. 20381.

[26] J. Ornik, M. Sakaki, M. Koch, J. C. Balzer, and N. Benson, "3D printed $A_{12}O_3$ for terahertz technology," *IEEE Access*, vol. 9, pp. 5986–5993, 2021, doi: 10.1109/ACCESS.2020.3047514.

[27] K.-D. Jenkel et al., "Effect of sintering temperature on the dielectric properties of 3D-printed alumina ($A_{12}O_3$) in the W-band," *J. Amer. Ceram. Soc.*, vol. 107, pp. 2494–2503, 2023.

[28] S. Biswas, "Design and additive manufacturing of broadband beam-forming lensed antennas and load bearing conformal antennas," Ph.D. dissertation, Dept. ECE, UDEL, Delaware, DE, USA, 2019.

[29] M. A. Elmansouri and D. S. Filipovic, "Wide-angle flattened Luneburg lens for millimeter-wave beam steering applications," in *Proc. IEEE Int. Symp. Phased Array Syst. Technol.*, 2022, pp. 01–06, doi: 10.1109/PAST49659.2022.9975017.

[30] P. E. Parsons, "Material development for functional additive manufacturing," Ph.D. dissertation, Dept. ECE, UDEL, Delaware, DE, USA, 2020.

[31] A. Jiménez-Sáez et al., "Temperature characterization of high-Q resonators of different materials for mm-wave indoor localization tag landmarks," in *Proc. 14th Eur. Conf. Antennas Propag.*, 2020, pp. 1–5, doi: 10.23919/EuCAP48036.2020.9135861.

[32] M. Schacht, N. Boukis, and E. Dinjus, "Corrosion of alumina ceramics in acidic aqueous solutions at high temperatures and pressures," *J. Mater. Sci.*, vol. 35, pp. 6251–6258, 2000.

[33] G. P. Pells, "Radiation damage effects in alumina," *J. Amer. Ceram. Soc.*, vol. 77, no. 2, pp. 368–377, 2005.

[34] S.-Y. Lin, V. M. Hietala, L. Wang, and E. D. Jones, "Highly dispersive photonic band-gap prism," *Opt. Lett.*, vol. 21, pp. 1771–1773, 1996.

[35] K. F. Brakora, J. Halloran, and K. Sarabandi, "Design of 3-D monolithic MMW antennas using ceramic stereolithography," *IEEE Trans. Antennas Propag.*, vol. 55, no. 3, pp. 790–797, Mar. 2007.

[36] D. R. Smith, Y. Urzhumov, N. B. Kundtz, and N. I. Landy, "Enhancing imaging systems using transformation optics," *Opt. Exp.*, vol. 20, no. 18, pp. 21238–21251, 2010.

[37] P. Kadera, J. Lacik, and H. Arthaber, "Effective relative permittivity determination of 3D printed artificial dielectric substrates based on a cross unit cell," *Radioengineering*, vol. 30, no. 4, pp. 595–610, 2021.

[38] P. Kadera and J. Lacik, "Effective complex permittivity measurement of 3-D printed artificial dielectric substrate based on a cross unit cell," in *Proc. 24th Int. Microw. Radar Conf.*, 2022, pp. 1–5.

[39] W. Wang, P. Lambert, and J. Chisum, "High-frequency limits for 3D-printed gradient-index (GRIN) lens antennas," in *Proc. EEE Int. Symp. Antennas Propag. USNC-URSI Radio Sci. Meeting*, 2023, pp. 1–2.

[40] S. K. Karki, J. Ala-Laurinaho, and V. Viikari, "Low-profile scanloss-reduced integrated metal-lens antenna," *IEEE Trans. Antennas Propag.*, vol. 70, no. 2, pp. 876–887, Feb. 2022, doi: 10.1109/TAP.2021.3111192.

[41] Z. Larimore, S. Jensen, A. Good, A. Lu, J. Suarez, and M. Mirotznik, "Additive manufacturing of Luneburg lens antennas using space-filling curves and fused filament fabrication," *IEEE Trans. Antennas Propag.*, vol. 66, no. 6, pp. 2818–2827, Jun. 2018, doi: 10.1109/TAP.2018.2823819.

[42] D. Nüßler and H.-H. Fuchs, "A Rotman lens at W-band," *Frequenz*, vol. 56, no. 11-12, pp. 244–248, Nov. 2002, doi: 10.1515/FREQ.2002.56.11-12.244.